ARTICLE

Robust Underwater Air Layer Retention and Restoration on *Salvinia*-Inspired Self-Grown Heterogeneous Architectures

Yachao Zhang, Yanlei Hu,* Bing Xu, Jianing Fan, Suwan Zhu, Yuegan Song, Zehang Cui, Hao Wu, Yi Yang, Wulin Zhu, Fengchao Wang, Jiawen Li, Dong Wu,* Jiaru Chu, and Lei Jiang

Read Online

ACCESS | Metrics & More | Article Recommendations | SI Supporting Information

ABSTRACT: *Salvinia's* long-term underwater air layer retention ability has inspired researchers to develop artificial microstructures. However, *Salvinia* has an exquisite combination of a complicated hollow structure and heterogeneous chemical properties, which makes artificial reproduction beyond the capabilities of traditional fabrication techniques. In addition, under extremely low underpressure conditions, the mechanism of retention and restoration of the underwater air layer of *Salvinia* remains unclear. Herein, by combining the shape memory polymer "top-constrained self-branching (TCSB)" and hydrophilic SiO₂ microspheres trapping, four-branch hollow microstructures with heterogeneous chemical properties are fabricated. By applying underpressure, the crucial role of hydrophilic apexes is unveiled in air layer restoration. Through the calculation of the surface energy, the underlying mechanism is well interpreted. This study holds great promise for developing *Salvinia*-inspired artificial structures and reveals the underlying mechanism of the robust air retention and recovery capability of *Salvinia* leaves in extreme environments.

KEYWORDS: *femtosecond laser fabrication, shape memory polymer, super-hydrophobic, Salvinia-inspired microstructures, air retention and restoration*
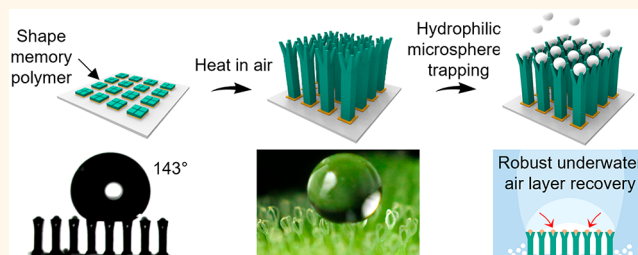
INTRODUCTION

Submerged in water, super-hydrophobic surfaces look like a perfect silvery mirror because of the air layer trapped between the microstructures. Such an underwater air layer has many applications, such as drag reduction,[1−4] anti-biofouling,[5,6] and anticorrosion.[7,8] However, the practicality is tempered by the poor air retention capability of lotus-inspired super-hydrophobic surfaces[9] under various disturbances, including liquid pressure,[10,11] fluid flow,[12,13] and air diffusion.[14,15] Interestingly, the floating water fern *Salvinia molesta* exhibits a robust underwater air retention ability even under extreme conditions with external disturbances such as floods. The distinct air retention ability is caused by the hydrophobic hollow structure composed of four multicellular hairs with hydrophilic apexes on the upper side of the leaf surface.[16]

Under real underwater conditions, turbulent flow, and hydrodynamic pressure can cause fluctuation and destruction of the flat air layer. Recent studies have explored the behavior of the underwater air layer of *Salvinia* under pressure changes.[17−19] Barthlott et al. found that the air bubbles trapped in the cavities at the top of the hollow structures help

to restore the air layer during the process of recovering from overpressure ($\Delta P = 600$ kPa) to normal pressure.[17] Xiang et al. demonstrated that the pinning effect of the hydrophilic heads of hollow structures is beneficial to the recovery of the air layer by external air replenishment at stationary overpressure ($\Delta P = 680$ kPa).[18] Gandyra et al. verified that apart from the pinning effect of the hydrophilic top, the entrapped air acts as a pneumatic spring, thereby enhancing the retention of the air layer at both low underpressure ($\Delta P = -6$ kPa) and overpressure ($\Delta P = 4$ kPa).[19] However, under the conditions of extremely low underpressure ($\Delta P \ll -6$ kPa) and subsequent recovery, the dynamic behavior of the underwater air layer of *Salvinia* remains uninvestigated, and the mechanism of air layer retention and restoration remains to be revealed.
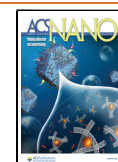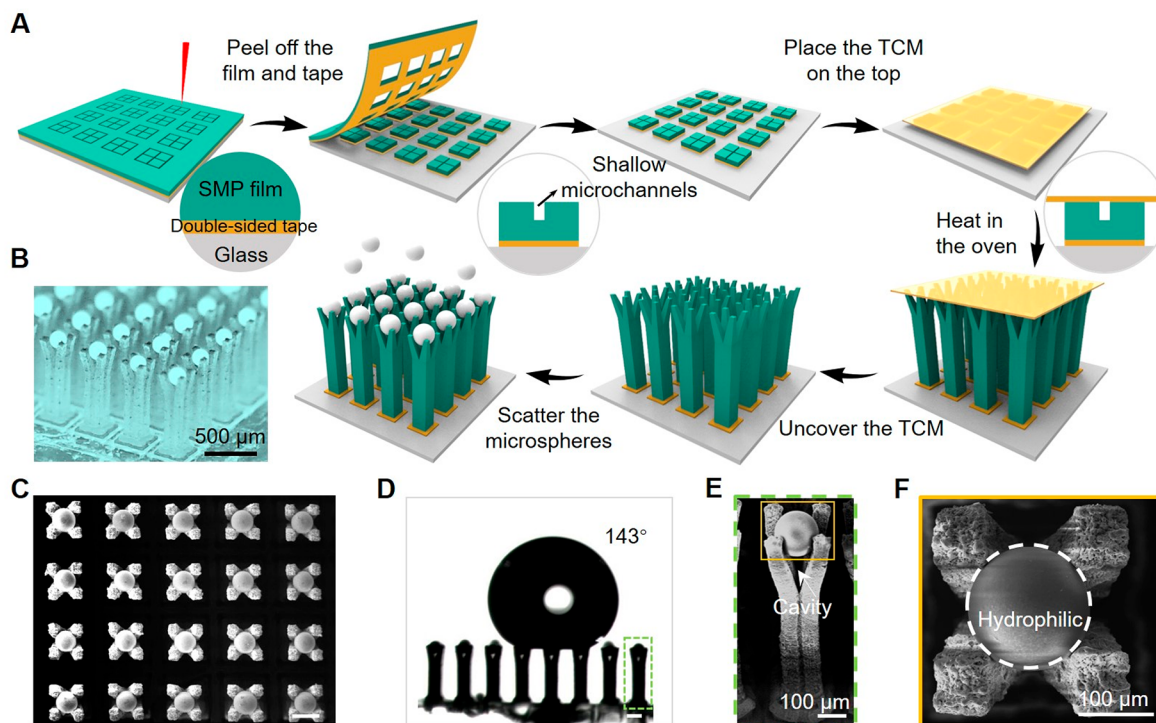
Figure 1. The TCSB method of fabricating *Salvinia*-inspired microstructures. (A) Schematic of the fabrication procedure for the BMCSs. The spacing between the pillars is ∼450 μm, and the height of the pillar is ∼1000 μm. The diameter of the hydrophilic SiO$_2$ microspheres is 150−200 μm. The dimensions of the microstructure are similar to those of the trichome of *Salvinia*. TCM: Top-constraining membrane. (B) Optical microscope image of BMCSs. Because of the defocus, the microspheres in the upper part of the image appear larger. (C) SEM image of BMCSs in (B). (D) The hydrophobic property of the BMCSs (WCA ≈ 143°). The scale bars in (C) and (D) are 200 μm. (E) Tilted-view SEM of a single BMCS. The cavity indicated by the white arrow is composed of a microsphere and branch. (F) Enlarged top-view SEM of BMCS. The white dashed circle indicates the hydrophilic SiO$_2$ microsphere.

Furthermore, unlike the thriving progress in *Salvinia* studies, the development of robust underwater air layer retention and restoration on *Salvinia*-inspired artificial surfaces is sluggish due to the lack of effective preparation methods.

From the view of fabrication, the fantastic combination of hierarchical structures with such heterogeneous super-hydrophobic surfaces and hydrophilic apexes makes the artificial reproduction of *Salvinia*-inspired microstructures a great challenge. Most of the previous studies mimicked either only the physical structure or chemical property, which limited their applications.[20] (1) Tricinci et al. fabricated hollow microstructures 100 repetitions smaller than those of natural *Salvinia* by direct laser lithography.[21] Applications in underwater hydrophobicity and localized water vapor condensation were studied. Yang et al. fabricated hollow microstructures comparable in size to those of *Salvinia* by immersed surface accumulation 3D printing.[22] Applications in droplet manipulation and oil/water separation were demonstrated. However, both structures fabricated by laser lithography and 3D printing were based on hydrophilic materials, and the air retention ability of the microstructures was not investigated. (2) Bhushan et al. fabricated micropillars (30 μm height) by photolithography, and then the top super-hydrophobic coating of the micropillar was stripped away with tape to achieve a hydrophilic tip.[23] Zheng et al. fabricated super-hydrophobic micropillars (∼50 μm height) with hydrophilic tops by using photolithography combined with electrodeposition.[24] On the one hand, they only investigated the water wetting property and adhesive force of the structure without studying the air retention ability. On the other hand, both structures were not

hollow in geometry and limited within the range of microscale, so they could only hold a small amount of air. Detailed discussion and comparison of the previous related works can be found in Figure S1. As a result, seeking a way to fabricate millimeter-scale hollow microstructures with hydrophilic tops and investigating the air retention and restoration ability of *Salvinia*-inspired structures are still challenges.

Here, a top-constrained self-branching (TCSB) method is developed to fabricate biomimetic super-hydrophobic four-branch microstructures, which are subsequently decorated with hydrophilic microspheres. Similar to the adult hairs of *Salvinia*, which grow from seedlings, the four-branch microstructures grow from shape memory microcubes. The height is made comparable to that of natural *Salvinia* hairs by controlling the heating time. Hydrophilic microspheres are stuck within the super-hydrophobic four-branch microstructures to mimic the heterogeneous chemical properties of *Salvinia* hairs. In addition, the cavities between the microspheres and branches mimic the hollow structure of *Salvinia* hairs. Thus, both the complicated hollow structure and the heterogeneous chemical properties of *Salvinia* are well replicated. Furthermore, the robust air retention and restoration capabilities of the natural *Salvinia* and our fabricated microstructures under overpressure and underpressure are quantified, respectively. It is verified that hydrophilic apexes play a key role in the air layer restoration of the extremely low underpressure-recovery process. By calculating the surface energy, the mechanism is well interpreted.
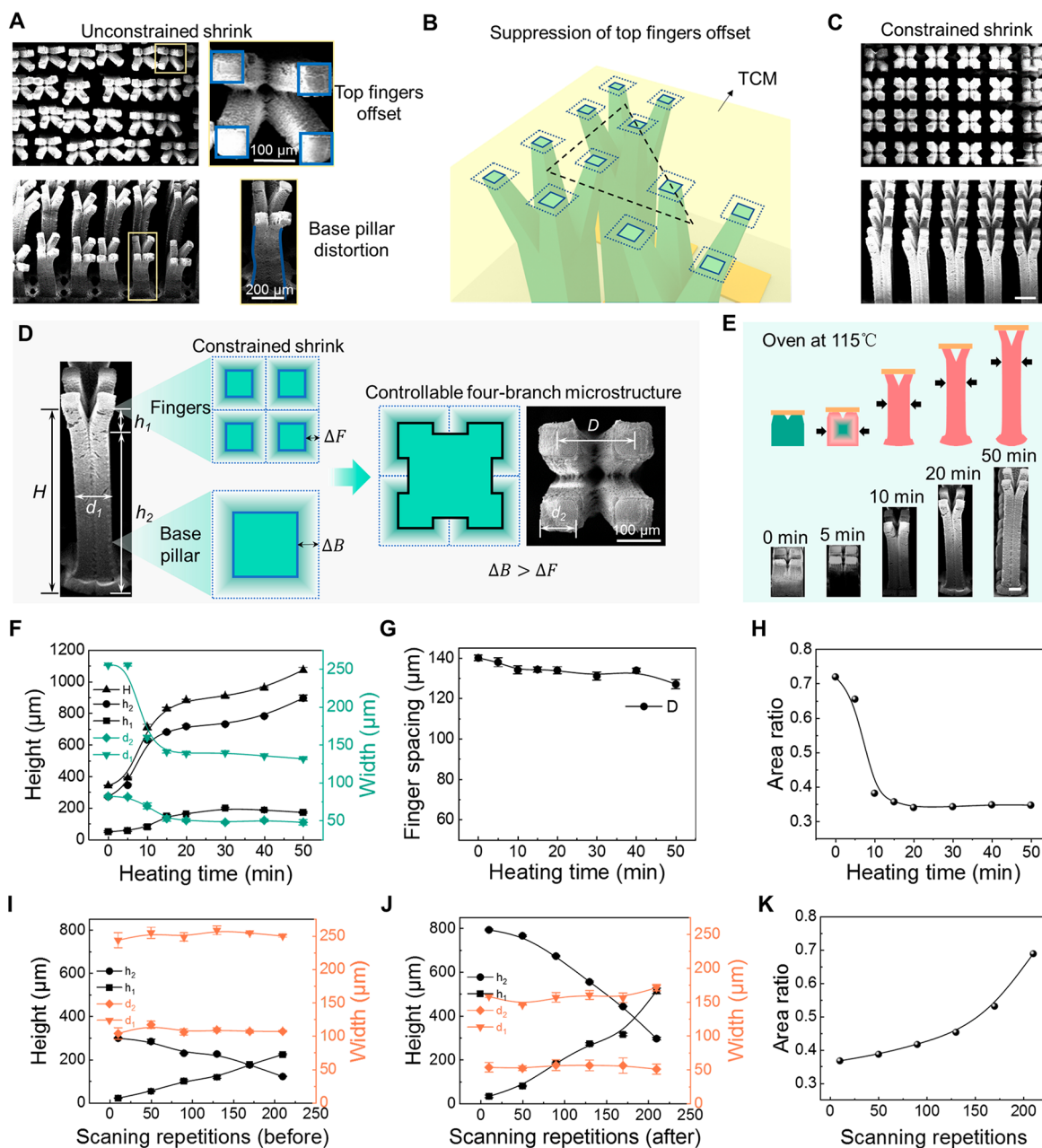
Figure 2. The interpretation of the TCSB mechanism and morphological control of microstructures. (A) Random shrinkage and growth of the microcube array after heating for 20 min without TCM. The top fingers decrease in size and deviate from their initial positions randomly. Meanwhile, the base pillars are distorted. (B) The TCM is attached to the microcube array to ensure that the fingers shrink concentrically and suppress the distortion of the base pillars. (C) Uniform shrinkage and growth of the microcube array with TCM after heating for 20 min. Scale bars: 200 μm. (D) The mechanism of self-branching with TCM. The contraction length of the base pillar is larger than that of the branch ($\Delta B > \Delta F$). (E) The heat shrinkable polystyrene microcube with microchannels on the top is heated in air at 115 °C from 0 to 50 min. Scale bar: 100 μm. (F–H) The morphology of the microstructure changes with heating time. The microchannels on the top of the microcube are scribed by a laser 50 repetitions. The sites measured for height, width, and finger spacing are shown in (D). (F) Quantitative relationship of the height and width of the microstructure with heating time. (G) Quantitative relationship of the finger spacing of the microstructure with heating time. (H) The area ratio of the microstructures decreases with heating time and stabilizes after 20 min. (I–K) The morphology of the microstructure changes with scanning repetitions when the heating time is fixed at 15 min. (I) Before heating, the quantitative relationship of the height and width of the microstructure with the scanning repetitions. (J) After heating, the quantitative relationship of the height and width of the microstructure with the scanning repetitions. (K) The area ratio of the microstructures increases with the scanning repetitions.

RESULTS AND DISCUSSION

Developing a TCSB Method for Fabricating *Salvinia*-Inspired Microstructures. The surface features of *Salvinia* are shown in Figure S2. The upper surface of the *Salvinia* leaf is covered with dense multicellular trichomes, and the water droplet beads up on the surface due to the hydrophobic property. Each hierarchical trichome is composed of a ~700 μm stalk and four hairs, which grow away from the stalk and finally connect at the apex and form a hollow structure. In addition to the complicated surface structure, the plant's
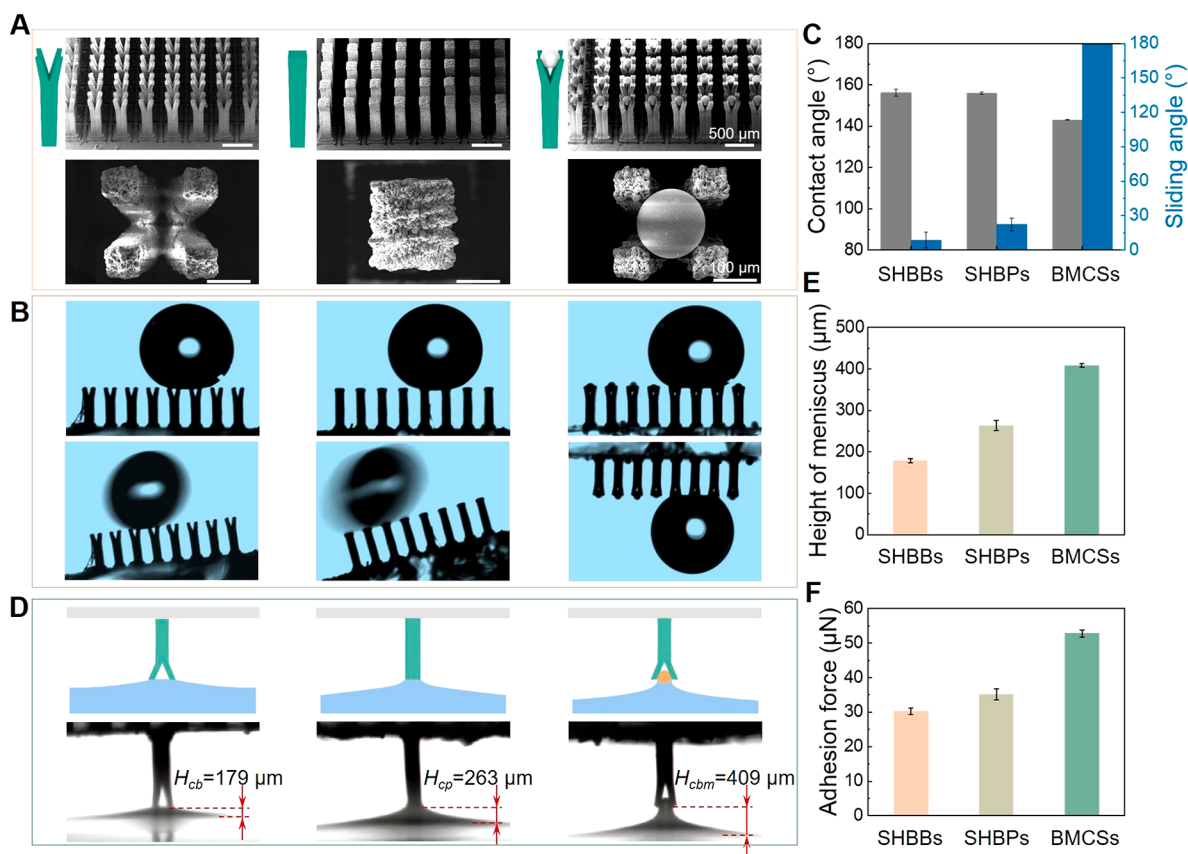
Figure 3. Quantitative comparison of wettability of three microstructures. First column is SHBBs. The second column is SHBPs. The third column is BMCSs. (A) The tilted-view SEM images of three microstructures and corresponding enlarged top-view SEM images. (B) The upper row is the image of a water droplet on the surface of different microstructures. The lower row is the image of a water droplet when it starts to roll by tilting the sample. The 4 μL water droplet sticks on the BMCSs even when the sample is turned upside down (petal effect). (C) The comparison of WCA and sliding angle for different microstructures. (D) Meniscus of three microstructures immediately before the snap-off. (E) The comparison of the height of the meniscus before the snap-off for three microstructures. (F) The calculated adhesive force of three microstructures according to the morphology of meniscus before the snap-off.

heterogeneous chemical property is also intriguing. On adult leaves, the dead terminal cell of each hair converges into a collapsed hydrophilic apex, while the overall leaf surface is covered with hydrophobic wax nanocrystals.

A TCSB method is developed to fabricate artificial *Salvinia* surfaces. Figure 1A shows a schematic process for fabricating branch-microsphere composite structures (BMCSs) in a shape memory polymer. The shape memory polymer used here is a 340 μm-thick heat shrinkable polystyrene film.[25−27] The film is attached to the glass substrate with double-sided tape. First, a femtosecond laser is adopted to scribe the 2D grid pattern on the shape memory film to form an array of isolated microcubes. Then, the laser is used to scribe cross shallow microchannels (50−80 μm) on the top of each microcube. The shape memory polymer film and tape then are peeled off, leaving the microcube array on the glass. Then, a top-constraining membrane (TCM) is placed on the sample, followed by heating in air at 115 °C for 15 min. After cooling, the TCM is removed, and a four-branch microstructure array is prepared. To achieve hydrophobic property, the sample is modified with fluorosilane. Then, the hydrophilic SiO₂ microspheres are scattered and trapped by branches (Figure S3). Finally, each branch traps a single microsphere (Figure 1B,C). Mechanical vibration and underwater ultrasonic cleaning experiments show that the microsphere trapping is robust (Figure S4). The 4 μL water contact angle (WCA) of BMCSs was measured and

found to be 143° (Figure 1D). The hollow feature and heterogeneous chemical property of the BMCS (Figure 1E,F) are similar to those of *Salvinia* leaves (Figure S2).

Owing to the flexibility of laser processing,[28−30] the initial microchannels on the top of microcubes can be easily tailored. As shown in Figure S5, various 2D geometrical patterns are designed for fabricating diverse branch microstructures, e.g., two-branch, six-branch, eight-branch, and round root with six-branch microstructures. Each structure in the array has the same height, demonstrating the validity of the top-constraining strategy. Equally, the hydrophilic SiO₂ microspheres can be trapped by a round root with six-branch microstructures, and the large area BMCS array is shown in Figure S6.

Interpretation of the TCSB Mechanism and Morphological Control of Microstructures. Owing to the drastic shape deformation of SMP during shrinkage, the SMP microcubes grow irregularly, and the formed microstructures are shown in Figure 2A and Video S1. Under an unconstrained heating condition, the top fingers decrease in size and deviate from their initial positions randomly. Meanwhile, the base pillars are distorted (Figures 2A and S7). To realize even shrinkage and growth, a "top-constraining" strategy is applied to restrain the lateral movement of the microcubes (Video S2). On the one hand, the fingers can only shrink concentrically *in situ* during heating since their tops are constrained by the TCM (Figure 2B). On the other hand, the TCM is restrained
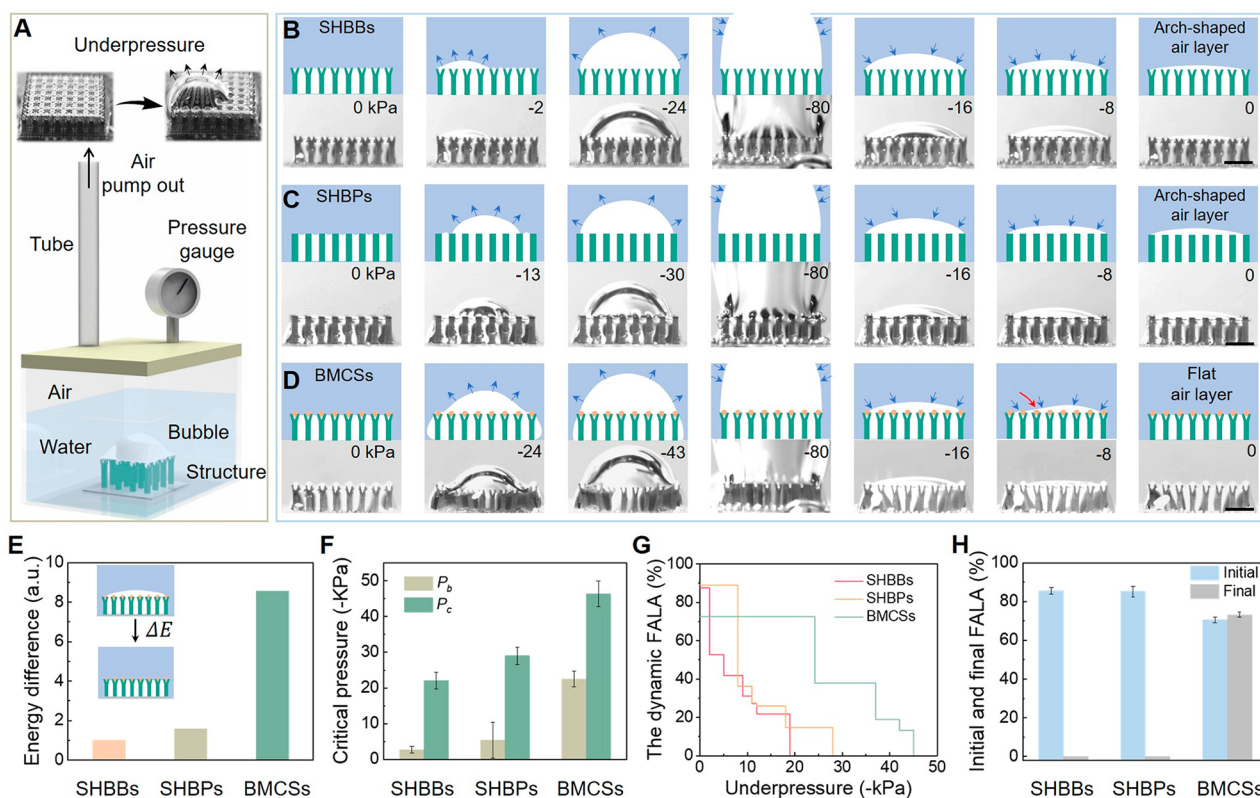
Figure 4. Underwater air layer retention and restoration ability of three microstructures under underpressure-recovery conditions. (A) Schematic of the underpressure test system. The CCD is horizontally mounted. The inset shows that the BMCS air layer breaks into an air cap during depressurization. (B–D) The changes in the AWI of three microstructures during depressurization and recovery. The blue arrows indicate the direction of the movement of the AWI. Scale bars: 1 mm. (B) The SHBBs. (C) The SHBPs. (D) The BMCSs. The first column is the initial state. The second column is the state in which the flat air layer starts to break. The third column is the state in which the air layer is completely broken. The fourth column is the state in which the pressure reaches the minimum (−80 kPa). The fifth to seventh columns show the recovery process, and the final pressure is recovered to normal. Only the AWI of BMCSs can recover to flat. The numbers indicate the current pressure compared to the standard atmospheric pressure. The red arrow in (D) indicates that the AWI is pinned by the hydrophilic microsphere. (E) Comparison of the surface energy differences between the arc-shaped air layer and the flat air layer of the three structures. The energy differences are normalized. (F) Comparison of the critical pressure when the air layer begins to break (P_b) and when it completely breaks (P_c) for the three microstructures. (G) The dynamic changes in the FALAs of different microstructures during depressurization. (H) Comparison of the FALAs before and after the depressurization-recovery test for the three microstructures.

in a horizontal plane owing to the neighboring supports of at least three microstructures; thus, the base pillar distortion is suppressed (Figure S8), and a uniform microstructure array is obtained (Figure 2C). The mechanism of self-branching with TCM is that both the fingers and base pillars shrink concentrically, while the base pillars shrink more freely compared with the top fingers ($\Delta B > \Delta F$, Figure 2D). Thus, a four-branch microstructure is formed.

To investigate the top-constrained self-branching process, the microcube with shallow microchannels on the top is heated at 115 °C from 0 to 50 min (Figure 2E). The temperature of the microcube increases and reaches the glass transition temperature (T_g) of the polystyrene film at 5 min. Then, the microcube starts to shrink and grow. The height of the branch pillar increases, while the width of the pillar shrinks. Figure 2F,G shows the quantitative relationship between heating time and the morphology of the branch pillar (the sites measured in regard to the width, height, and finger spacing are indicated in Figure 2D). The SEM images of the microstructure are shown in Figure S9. Before heating, the overall height (H) of the pillar is 340 μm, which is equal to the thickness of the polystyrene film (Figure 2F). As the heating time increases, the widths of the finger (d_2) and base pillar (d_1) decrease because of the

increasing extent of shrinkage. After 20 min, the widths of the finger and base pillar gradually stabilize at 50 and 135 μm, respectively. Accordingly, the height increases with heating time. The finger height (h_1) stabilizes at 180 μm after 20 min, while the base height (h_2) increases consistently to 900 μm for 50 min. The center-to-center finger spacing (D) slightly decreases from 140 to 127 μm (Figure 2G). Here, the area ratio is defined as the percentage of structure area extracted from the SEM images (Figure S9). As shown in Figure 2H, the area ratio decreases from 0.72 with heating time and finally stabilizes at 0.35 after 20 min, indicating that the sizes of the top parts of the branches are nearly unchanged after 20 min.

Figure 2I,J shows the quantitative relationship between the laser scanning repetitions and the morphology of the branch pillar. The SEM images of the microstructure are shown in Figure S10. Before heating, the finger height increases from 21 to 223 μm, and the base height decreases to 121 μm with increasing scanning repetitions. The finger width and base width are 110 and 250 μm, respectively (Figure 2I). After heating for 15 min, the finger grows to 513 μm with 210 laser scanning repetitions (Figure 2J). It is worth noting that the finger gradually bends when the scanning repetitions are larger than 90 (Figure S10). Accordingly, the finger width and base

width shrink to 55 and 160 μm, respectively. Meanwhile, the area ratio increases with the scanning repetitions since the fingers bend and take up the space between the pillars (Figures 2K and S10). Furthermore, the relationship between heating temperature and the growth of the polymer is also studied (Figure S11).

Quantitative Comparison of the Wettability of the Three Microstructures. Furthermore, three different structures, termed super-hydrophobic branches (SHBBs), super-hydrophobic pillars (SHBPs), and branch-microsphere composite structures (BMCSs), are fabricated to characterize their underwater air layer retention and restoration ability (Figure 3A). As shown in Figure 3B,C, the WCAs of the SHBBs and SHBPs are both above 155°. Because the solid−water contact area of SHBPs is much larger than that of SHBBs (Figure S12), the water sliding angle of SHBPs (22.3°) is larger than that of SHBBs (8.6°). After hydrophilic microspheres are trapped, the super-hydrophobic property of the branches is changed to hydrophobic (143°). The BMCSs show a good controllability of water droplet even when turned upside down. Water cannot penetrate into the microcavity composed of the microsphere and four fingers owing to the super-hydrophobicity of branches. The hydrophilic apexes at the tips of the *Salvinia* trichomes have been deemed to benefit air layer stabilization by pinning the air−water interface (AWI). The adhesive force of the hydrophilic apex plays a key role in the pinning effect. Here, the adhesive force of the fabricated tips is investigated using the capillary adhesion technique (Figures 3D and S12).[19,22,31] The height of the meniscus before the meniscus snap-off is termed the critical height (H_c). As shown in Figure 3E, the critical height of SHBB (H_{cb}) is the smallest (179 μm) among all the structures because of its low surface energy property and the smallest water−solid contact area. The critical height of the BMCS (H_{cbm}) is the largest (409 μm) since water can wet the surface of the microsphere. According to the height of the meniscus before snap-off, the adhesive force is calculated (Figure 3F). The adhesive force of the BMCS is 52.8 μN, which is 2.7 times larger than that of the single trichome on *Salvinia* leaves.[31]

Underwater Air Layer Retention and Restoration of Natural and Artificial Samples under Underpressure-Recovery Conditions. A homemade apparatus consisting of a commercial vacuum chamber, pressure gauge valve, air pump, and CCD is built to perform underpressure characterization (Figures 4A and S13). To systematically investigate the changes in the air−water interface (AWI) and flat air layer area (FALA, the proportion of the unbroken flat air layer area to the initial air layer area), we monitored the real-time dynamic process at different titled view angles of 90° and 60° (Figures S14 and S15).

Change in AWI of Natural Salvinia. The whole process is shown in Video S3, and the screenshots are shown in Figure S14. There is a flat AWI on the top of the trichomes at 0 kPa. At −2 kPa, the initial AWI begins to break, and a small air cap is formed. As the pressure decreases, a large bubble spreads over the whole surface at −35 kPa. The pressure is continuously decreased to −50 kPa and then starts to recover to normal pressure (standard atmospheric pressure). The bubble gradually shrinks, and the AWI partially contacts the top of the trichomes at −13 kPa. When the pressure returns to 0 kPa, the AWI becomes flat again. The recovered air layer is same as the initial air layer, indicating the robust air layer restoration of *Salvinia* leaves.

Change in AWI of Artificial Samples. Same as natural *Salvinia*, once the artificial sample is placed underwater, a silvery appearance of the air layer is observed (inset in Figure 4A). The whole process is shown in Videos S4, S5, and S6, and the screenshots are shown in Figure 4B−D. As shown in Figure 4B and Video S4, there is a flat AWI on top of the SHBBs at 0 kPa. At −2 kPa, the initial AWI begins to break, and a small air cap is formed. As the pressure decreases, a large bubble spreads over the whole surface at −24 kPa. The air is continuously pumped out until −80 kPa. Finally, the valve is opened slowly to let the air in. The bubble gradually shrinks into an arch-shaped air layer (Figure S15). For the SHBPs (Figure 4C and Video S5), the dynamic process of the AWI is similar. The first breakage and full breakage of the AWI are at −13 kPa and −30 kPa, respectively, which are larger than those of the SHBBs due to the higher adhesive force (Figure 3F). The surface energy difference (ΔE) between the arc-shaped air layer and the flat air layer is calculated (Figures 4E and S16). For the SHBBs and SHBPs, the ΔE_{SHBBs} and ΔE_{SHBPs} are small. The initial flat air layers of the SHBBs and SHBPs are in a metastable state, and they are easily broken into arc-shaped air layers under small disturbances. In the recovery process, the air layer cannot be pinned by the tops of the SHBBs and SHBPs, and thus, the flat air layer cannot recover. For BMCSs (Figure 4D and Video S6), the spaces between the branches are filled with air, which is the same as Figure 4B, and only the microspheres are wetted by the water. During depressurization, the bubbles first form and grow larger on the sides of the array and then migrate to the top because the top surface has the highest adhesive force (Figure 3F). The AWI begins to break at −24 kPa, and the bubble spreads across the whole surface at −43 kPa, which is a much larger value than those of SHBBs and SHBPs, owing to the pinning effect of the hydrophilic microspheres. The ΔE_{BMCSs} is the largest among the three structures, and thus, the arc-shaped air layer (high energy state) spontaneously recovers to a flat air layer (low energy state), which is the same process that occurs with natural *Salvinia* (Figure S14). In the recovery process, once the AWI comes into contact with the hydrophilic microspheres, the AWI can be pinned, and the flat air layer can be gradually recovered. The experimental results for different samples are shown in Figure S17. Two critical pressure values are defined to quantitatively characterize the air layer retention ability. One is P_b, under which the AWI begins to break. The other is termed P_c, under which the AWI is completely broken. A comparison of these two values for the three structures is shown in Figure 4F. Both the values of the BMCSs are much larger than those of the SHBBs and SHBPs.

Dynamic FALA of Artificial Samples. Owing to the surface structures of *Salvinia* having varied sizes and spacings, it is hard to measure the FALA accurately. For the artificial samples which have uniform size and spacing, the dynamic change in FALA is clearly recorded (Videos S7, S8, and S9). As shown in Figure 4G, the initial FALA values of the SHBBs and SHBPs are 87.5% and 88.8%, respectively, while the value for the BMCSs is 72.4% because the microspheres are wetted by water. The critical pressure values in which the first breakage occurs for the SHBBs and SHBPs are −2 kPa and −8 kPa, and the corresponding FALA values decrease to 52.7% and 36.2%, respectively. However, for the BMCSs, the FALA remains at 72.4% even at −8 kPa. As the pressure decreases to −24 kPa, the FALAs of the three structures are 0%, 14.7%, and 38%. The FALA decreases to zero at −19 kPa (SHBBs), −28 kPa (SHBPs), and −45 kPa (BMCSs). The FALAs of the three
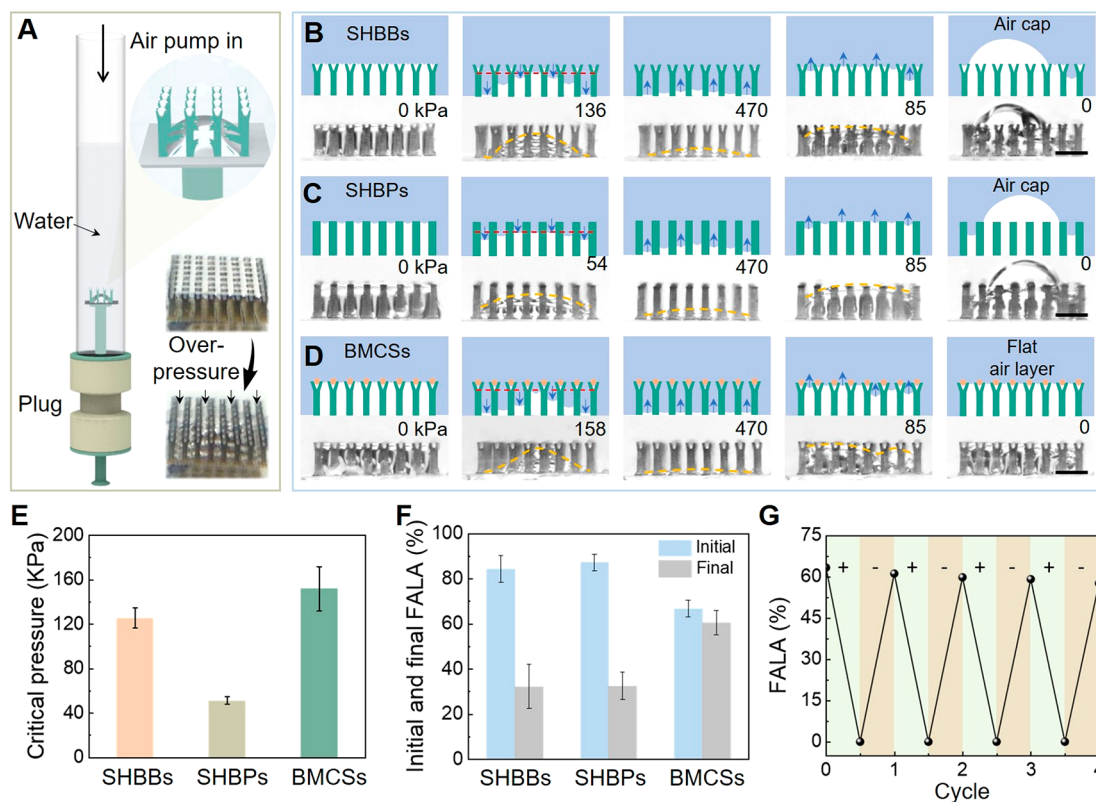
Figure 5. The underwater air layer retention and restoration ability of the three microstructures under overpressure-recovery conditions. (A) Schematic of the overpressure test system. The CCD is horizontally mounted. The inset is an optical image of the BMCS air layer after applying overpressure. (B−D) The changes in the AWI of three microstructures under pressurization and recovery conditions. The blue arrows indicate the direction of the movement of the AWI. The yellow dashed lines in (B−D) indicate the AWI. Scale bars: 1 mm. (B) The SHBBs. (C) The SHBPs. (D) The BMCSs. The first column is the initial state. The second column is the state in which the AWI is completely broken (when the AWI is lower than the red dashed line). The third column is the state in which the pressure reaches the maximum (470 kPa). The fourth and fifth columns show the recovery process, and the final pressure is recovered to normal. Only the AWI of BMCS can recover to flat. The SHBBs and SHBPs are partially wetted by water, and air caps are formed on the surface. The numbers indicate the current pressure. (E) Comparison of the critical pressure when the air layer is fully broken for different microstructures. (F) Comparison of the FALA before and after the pressurization-recovery test for different microstructures. (G) The change in the FALA of BMCSs during four pressurization-recovery tests.

structures before and after the depressurization-recovery test are quantitatively compared in Figure 4H. As the pressure is recovered, the FALA of the BMCSs is nearly unchanged (∼70%). In contrast, both the FALA of the SHBBs and that of the SHBPs are zero because of the arch-shaped air layer. The promising extremely low underpressure-resistance and recovery abilities of the air layer demonstrate the superiority of *Salvinia*-inspired BMCSs compared with super-hydrophobic surfaces.

Underwater Air Layer Retention and Restoration of Natural *Salvinia* and Artificial Samples under Overpressure-Recovery Conditions. A homemade device consisting of a transparent plastic tube with one end sealed with a plug, air pump, and CCD was used to explore the effect of overpressure on the air layer of natural *Salvinia* and our fabricated structures (Figures 5A and S18 and S19). The pressure was increased at 20 kPa per second with a maximum of 470 kPa for safety reasons.

Change in the AWI of Natural Salvinia. The initial flat AWI starts to break at 20 kPa (Figure S19 and Video S10). At 280 kPa, the AWI is fully detached from the top of the trichomes and compressed to the substrate, while air in the cavities of the hollow structures is still observed. The pressure is continuously increased to 470 kPa, and the air in the cavities

collapses to form small bubbles. Then, the pressure starts to recover to normal pressure. The air between the trichomes and in the cavities recovers simultaneously. The stalks of the trichomes provide a frame for the vertical movement of the three-phase-contact lines (TCLs). When the TCLs rise enough to contact the bubbles in the cavities, the bubbles merge into the air layer, and the TCLs move instantaneously to the top of the trichomes (at 105 kPa). Thus, the air in the hollow structure of *Salvinia* is in favor of the air layer restoration. Because of the nonuniform sizes of the trichomes, the TCLs have different movement speeds but eventually pin at the top of the trichomes.[18] Finally, the AWI is recovered and is the same as the original flat shape (at 0 kPa), demonstrating the robust air layer restoration of *Salvinia* leaves.

Change in the AWI of SHBBs. As shown in Figure 5B and Video S11, water penetrates into the structure array from the edge to the center, and the air layer around the array is suppressed to the substrate first. The AWI in the center remains stable until it breaks completely at 136 kPa (the pressure when the AWI is lower than the branches, which is indicated by the red dashed line). As the pressure increases, the water moves toward the center, and the air layer is fully compressed to the substrate. Then, the pressure is lowered by opening the valve slowly. The air between the fingers and the

base pillars recovers simultaneously (Figure S20). The base pillars provide a frame for the vertical movement of TCLs. Since the AWI is intersected by the base pillars, the resistance distributes along the circumference of the branch pillar in the vertical direction (F_{slide}). When the TCLs rise enough to contact the bubble in the cavities, the bubble merges into the air layer, which is the same process that occurs with natural *Salvinia*. The TCLs in the center arrive early, while the TCLs in the corner are hindered by F_{slide}. Because of the low adhesive force of the top of SHBBs ($F_{b,top}$), the early arriving TCLs detach from the apexes, and an air cap is formed on the surface (Figure S21).

Change in AWI of SHBPs. Compared with a branch structure, the straight pillar decreases the energy required for water penetration, and thus the air layer is completely broken at 54 kPa, indicating that the straight pillar structure is inferior to the branches (136 kPa) in terms of retaining the air layer (Figure 5C and Video S12). For the same reason as that of the SHBBs, an air cap is formed when the pressure returns to normal.

Change in AWI of BMCSs. As shown in Figure 5D and Video S13, the suppression of the AWI is the same as that of the SHBBs. The air layer is completely broken at 158 kPa, which is much larger than that of SHBPs (54 kPa). The better air layer retention ability is attributed to the multibranch structures, which increase the area to be wetted; thus, the energy required for water penetration is increased.[16] Because of the pinning effect of the hydrophilic microspheres, the pinning force of the top $F_{m,top}$ is higher than the sliding resistance F_{slide}. The early arriving TCLs are pinned to the tops of the structures. Finally, the air expels the water, and a flat AWI is recovered, which is the same process that occurs with natural *Salvinia* (Figure S21). The critical pressure values of the three structures when the air layer is completely broken are compared in Figure 5E. The critical pressure of the BMCSs is the highest (151.9 kPa). The experimental results for different samples are shown in Figure S22.

Change in FALA of Artificial Samples. A 60° tilted CCD is used to record the FALA change before and after the pressurization-recovery test (Figure S23 and Videos S14, S15, and S16). As shown in Figure 5F, owing to the wetted hydrophilic microspheres, the initial FALA of the BMCSs is the lowest (66.8%) compared with those of the SHBBs (84.4%) and SHBPs (87.2%). However, after recovery, only the air layer of BMCSs can be recovered (60.7%), while an air cap is formed on the SHBBs (32.3%) and SHBPs (32.6%). Two reasons account for the slight decrease in the FALA in BMCSs. On the one hand, part of the surface is wetted after pressurization. On the other hand, air dissolution is increased under high pressure. Four pressurization and recovery cycles are carried out with BMCSs at 470 kPa (Figures 5G and S24). After the four cycles, the FALA decreases slightly from 63.4% to 57.7%, and no air cap is formed, thereby demonstrating the robustness of air layer retention and restoration of the fabricated composite surface.

Furthermore, to investigate the longevity, as shown in Figure S25, repeating overpressure-recovery and underpressure-recovery characterization was done with one BMCS (Sample 4 in Figure S3D). Because of the solubility of the air increases with pressure, the air in the sample is gradually dissolved by water[10] (Figure S25B). After 39 pressurization-recovery cycles, the flat air layer area (FALA) decreased from 70.6% to 4.9% (Figure S25C). During the repeating cycles, the air layer was

recovered to be flat every time, showing that the hydrophilic microspheres are not depleted. The sample was then taken out and placed underwater again (Figure S25D). Since some super-hydrophobic nanoparticles were deposited on the surface of hydrophilic SiO_2 microspheres and branches during the repeating overpressure-recovery cycles (Figure S26), the hydrophilicity of SiO_2 microspheres was weakened, and the FALA increased to 87.3% (Figure S25D). To perform the underpressure-recovery experiment, the pressure was decreased to −80 kPa,= and then increased to 0 kPa repeatedly. The air in the water merged into the sample with each cycle as air solubility decreased with pressure (Figure S25E). The red ellipses indicate that the air volume in the sample increased (Figure S25D). After eight cycles, the pressure inside the sample was larger than the adhesion force of hydrophilic microspheres, and the flat air layer cannot be recovered and the FALA decreased to 60.8%. If the sample is taken out and placed under water, the air layer can recover to flat again. Continuously, after 6−9 cycles, the flat air layer was broken and the FALA decreased (Figure S25F). When the pressure is only reduced to −30 kPa, the air in the water is hardly merged into the sample in each cycle, as air solubility is little changed at this low underpressure. The air layer can always recover to flat, and the FALA changes little after repeating 55 cycles, demonstrating the robustness of hydrophilic microspheres (Figure S27).

CONCLUSION

A TCSB method is proposed to achieve *Salvinia*-inspired complicated hollow architectures and heterogeneous chemical properties. The mechanism underlying this self-branching phenomenon is investigated. Hydrophilic microspheres are scattered and held by the branches to mimic the heterogeneous chemical properties of *Salvinia*. By applying underpressure and overpressure on BMCSs, respectively, the different roles played by the four-branch structures and hydrophilic apexes in air layer retention and restoration are systematically investigated. The four-branch structures are in favor of preventing water penetration (or retaining air layer) compare to straight pillars. The hydrophilic apexes help to retain the air layer under the underpressure conditions, as well as recover the air layer in the recovery process of overpressure conditions. Interestingly, the crucial role of hydrophilic apexes is unveiled in air layer restoration during the extremely low underpressure-recovery process. In brief, regardless of which direction the AWI approaches the topmost level of the surface, the hydrophilic apexes help to recover the air layer. By calculating the surface energy, the mechanism of robust air layer restoration under extremely low underpressure-recovery conditions is well interpreted. The elasticity of the trichomes of *Salvinia* provides a buffer against the slight deformation of the AWI. Here, the material we use is a rigid-shaped memory polymer, and developing the TCSB method with soft material is our future work. With the integration of the elasticity, the air retention and restoration performance may be further improved. Our study not only holds great promise for fabricating functional microstructures with great scalability and flexibility but also offers a deep understanding of the robust air retention and recovery ability of *Salvinia* leaves, which promote the wide underwater applications of air-retaining surfaces.

EXPERIMENTAL SECTION

Materials and Equipment. *Salvinia* leaves were purchased from the Yufeng flower market (Hefei, China). The heat shrinkable polystyrene shape memory film was purchased from Dongguan Nogard Arts & Crafts Factory. Double-sided tape (Kapton, TED PELLA Inc., USA) was used to adhere the SMP film to a glass substrate, and the same tape was also applied as a top-constraining membrane to constrain the top of the polystyrene microcube during heating. The SiO_2 microspheres were purchased from Knowledge & Benefit Sphere Tech. Co., Ltd., whose diameter ranges from 150 to 200 μm. Before the microspheres were trapped, the super-hydrophobic nanoparticles were sprayed coated on the four-branch micropillars to reduce the adhesion between the SiO_2 microspheres and the branch structure and substrate to facilitate microspheres trapping; thus, the SiO_2 microspheres that are not trapped by the branch can be easily removed by air blowing. The SiO_2 microspheres were scattered on the branches, and then a glass plate was used to push them into the branches. The fingers of the branches are deformed to hold the microspheres tightly. The microspheres that were not trapped by the branches were removed by blowing air across the surface. After several "scattering—pushing—blowing" cycles, each branch trapped a single microsphere. The vacuum chamber with an air pump used in the underpressure test was purchased from Zhangjiagang ZongChi Machine Equipment Co., Ltd. A digital camera (PowerShot SX600HS, Cannon, Japan) equipped with a macro lens (EF 100 MM IS USM, Cannon) was used to take photos of the *Salvinia Molesta* and record the change in the air layer of the sample. A CCD (Mindvision) equipped with a macro lens (HY-180XA) was used to record the change in the AWI. The overpressure test system is composed of a transparent plastic tube and a detachable plug. The sample is placed on the horizontal stage, which is combined with the plug. Only one end of the tube had water, and the sample was submerged at a depth of 5 cm. An electronic air pump (TD3, TCL Inc.) was used to inflate air into the tube and generate hydrodynamic pressure on the sample.

Femtosecond Laser Fabrication Method. The laser beam (104 fs, 1 kHz, 800 nm) was generated by a regenerative amplified Ti:sapphire femtosecond laser system (Legend Elite-1K-HE, Coherent, USA). Through a galvoscanner system (SCANLAB, Germany) equipped with a telecentric f-theta lens (focal length = 63 mm), the laser beam was guided onto the polystyrene film surface. The scanning path was designed by AutoCAD 2014 and then imported into the processing software (Samlight). The scanning sequence is the same as the drawing sequence, which can be changed easily. By combining a half-wave plate and a low dispersion polarizer, the laser power can be adjusted. The scanning speed and scanning repetitions were controlled by Samlight software.

Characterization. SEM images were taken with a scanning electron microscope (FEI, Sirion 200) operated at 10 kV after the samples were sputtered with Au for 120 s. An optical microscope (LW200−3JT) was used to observe the microstructures. The WCA was measured by a CA100C contact-angle system (Innuo, China).

ASSOCIATED CONTENT

ⓢ Supporting Information

The Supporting Information is available free of charge at https://pubs.acs.org/doi/10.1021/acsnano.1c09669.

Figures S1−S27: comparison of our work with the cited literature, surface features of the *Salvinia*, microspheres trapping by four-branch, mechanical stability characterization of the captured microspheres, multibranch micropillars, microspheres trapping by six-branch, self-growth, and self-branching processes with or without TCM during heating, suppression of the base pillar distortion with the TCM, branch arrays with increasing heating time, branch arrays with increasing laser scanning repetitions, influence of the heating temperature on the polymer shrinkage and growth, capillary adhesion force measurement of three structures, homemade apparatus for underpressure characterization, air layer recovery of natural *Salvinia* leaves under underpressure-recovery conditions, tilted view of the underwater air layer of three microstructures under underpressure-recovery conditions, calculation of the surface energy for the three structures, air layer change of the three microstructures under the underpressure-recovery conditions of different samples, homemade apparatus for overpressure characterization, air layer recovery of natural *Salvinia* leaves under overpressure-recovery conditions, restoration of the air layers of the three structures in the recovery of overpressure test, pinning effect of the hydrophilic spheres in the air layer restoration of the overpressure test, air layer changes of the three microstructures under overpressure-recovery conditions for different samples, underwater air layers of the three microstructures under overpressure-recovery conditions, four pressurization and recovery cycles carried out on BMCSs, repeating underwater air layer retention and restoration under overpressure-recovery and underpressure-recovery conditions, comparison of the morphology of branch and microsphere before and after repeating test, and repeating test under underpressure ($−30$ kPa)-recovery conditions (PDF)

Movie of underwater air layer retention and restoration of the *Salvinia* under the underpressure-recovery conditions (MP4-1)

Movie of underwater air layer retention and restoration of the *Salvinia* under the overpressure-recovery conditions (MP4-2)

Movie of the self-growth and self-branch process without the top-constraining membrane (TCM) (MP4-3)

Movie of the self-growth and self-branch process with the top-constraining membrane (TCM) (MP4-4)

Movie of underwater air layer retention and restoration of the SHBBs under the underpressure-recovery conditions (MP4-5)

Movie of underwater air layer retention and restoration of the SHBPs under the underpressure-recovery conditions (MP4-6)

Movie of underwater air layer retention and restoration of the BMCSs under the underpressure-recovery conditions (MP4-7)

Movie of tilted view of air layer of SHBBs under the underpressure-recovery conditions (MP4-8)

Movie of tilted view of air layer of SHBPs under the underpressure-recovery conditions (MP4-9)

Movie of tilted view of air layer of BMCSs under the underpressure-recovery conditions (MP4-10)

Movie of underwater air layer retention and restoration of the SHBBs under overpressure-recovery conditions (MP4-11)

Movie of underwater air layer retention and restoration of the SHBPs under overpressure-recovery conditions (MP4-12)

Movie of underwater air layer retention and restoration of the BMCSs under overpressure-recovery conditions (MP4-13)

Movie of tilted view of air layer of SHBBs under overpressure-recovery conditions (MP4-14)

Movie of tilted view of air layer of SHBPs under overpressure-recovery conditions (MP4-15)

Movie of tilted view of air layer of BMCSs under overpressure-recovery conditions (MP4-16)

AUTHOR INFORMATION

Corresponding Authors

Yanlei Hu − *CAS Key Laboratory of Mechanical Behavior and Design of Materials, Key Laboratory of Precision Scientific Instrumentation of Anhui Higher Education Institutes, Department of Precision Machinery and Precision Instrumentation, University of Science and Technology of China, Hefei 230027, China;* ⓘ orcid.org/0000-0003-1964-0043; Email: huyl@ustc.edu.cn

Dong Wu − *CAS Key Laboratory of Mechanical Behavior and Design of Materials, Key Laboratory of Precision Scientific Instrumentation of Anhui Higher Education Institutes, Department of Precision Machinery and Precision Instrumentation, University of Science and Technology of China, Hefei 230027, China;* ⓘ orcid.org/0000-0003-0623-1515; Email: dongwu@ustc.edu.cn

Authors

Yachao Zhang − *CAS Key Laboratory of Mechanical Behavior and Design of Materials, Key Laboratory of Precision Scientific Instrumentation of Anhui Higher Education Institutes, Department of Precision Machinery and Precision Instrumentation, University of Science and Technology of China, Hefei 230027, China;* ⓘ orcid.org/0000-0002-4468-6142

Bing Xu − *School of Mechanical Engineering, Suzhou University of Science and Technology, Suzhou 215009, China*

Jianing Fan − *Department of Modern Mechanics, CAS Center for Excellence in Complex System Mechanics, University of Science and Technology of China, Hefei 230027, China*

Suwan Zhu − *CAS Key Laboratory of Mechanical Behavior and Design of Materials, Key Laboratory of Precision Scientific Instrumentation of Anhui Higher Education Institutes, Department of Precision Machinery and Precision Instrumentation, University of Science and Technology of China, Hefei 230027, China;* ⓘ orcid.org/0000-0001-9881-5694

Yuegan Song − *Key Laboratory of Testing Technology for Manufacturing Process of Ministry of Education, Southwest University of Science and Technology, Mianyang 621010, China*

Zehang Cui − *CAS Key Laboratory of Mechanical Behavior and Design of Materials, Key Laboratory of Precision Scientific Instrumentation of Anhui Higher Education Institutes, Department of Precision Machinery and Precision Instrumentation, University of Science and Technology of China, Hefei 230027, China*

Hao Wu − *CAS Key Laboratory of Mechanical Behavior and Design of Materials, Key Laboratory of Precision Scientific Instrumentation of Anhui Higher Education Institutes, Department of Precision Machinery and Precision Instrumentation, University of Science and Technology of China, Hefei 230027, China*

Yi Yang − *CAS Key Laboratory of Mechanical Behavior and Design of Materials, Key Laboratory of Precision Scientific Instrumentation of Anhui Higher Education Institutes, Department of Precision Machinery and Precision Instrumentation, University of Science and Technology of China, Hefei 230027, China; Key Laboratory of Testing Technology for Manufacturing Process of Ministry of Education, Southwest University of Science and Technology, Mianyang 621010, China*

Wulin Zhu − *CAS Key Laboratory of Mechanical Behavior and Design of Materials, Key Laboratory of Precision Scientific Instrumentation of Anhui Higher Education Institutes, Department of Precision Machinery and Precision Instrumentation, University of Science and Technology of China, Hefei 230027, China*

Fengchao Wang − *Department of Modern Mechanics, CAS Center for Excellence in Complex System Mechanics, University of Science and Technology of China, Hefei 230027, China;* ⓘ orcid.org/0000-0002-5954-3881

Jiawen Li − *CAS Key Laboratory of Mechanical Behavior and Design of Materials, Key Laboratory of Precision Scientific Instrumentation of Anhui Higher Education Institutes, Department of Precision Machinery and Precision Instrumentation, University of Science and Technology of China, Hefei 230027, China;* ⓘ orcid.org/0000-0003-3950-6212

Jiaru Chu − *CAS Key Laboratory of Mechanical Behavior and Design of Materials, Key Laboratory of Precision Scientific Instrumentation of Anhui Higher Education Institutes, Department of Precision Machinery and Precision Instrumentation, University of Science and Technology of China, Hefei 230027, China;* ⓘ orcid.org/0000-0001-6472-8103

Lei Jiang − *Key Laboratory of Bio-inspired Materials and Interface Sciences, Technical Institute of Physics and Chemistry, Chinese Academy of Sciences, Beijing 100190, China;* ⓘ orcid.org/0000-0003-4579-728X

Complete contact information is available at:
https://pubs.acs.org/10.1021/acsnano.1c09669

Author Contributions

Y.Z., Y.H., and D.W. conceived the concept of the research. Y.Z., B.X., Y.S., H.W., Z.C., Y.Y., and W.Z. performed the experiments. Y.Z., Y.H., J.F., S.Z., F.W., D.W., J.L., J.C., and L.J. analyzed the data and prepared the manuscript. J.L., D.W., Y.H., J.C., and L.J. reviewed and revised the manuscript. All authors commented on the paper.

Notes

The authors declare no competing financial interest.

ACKNOWLEDGMENTS

REFERENCES

(1) Lee, C.; Choi, C.-H.; Kim, C.-J. Superhydrophobic Drag Reduction in Laminar Flows: A Critical Review. *Exp. Fluids* **2016**, *57*, 176.

(2) Hu, H.; Wen, J.; Bao, L.; Jia, L.; Song, D.; Song, B.; Pan, G.; Scaraggi, M.; Dini, D.; Xue, Q.; Zhou, F. Significant and Stable Drag Reduction with Air Rings Confined by Alternated Superhydrophobic and Hydrophilic Strips. *Sci. Adv.* **2017**, *3*, No. e1603288.

(3) Daniello, R. J.; Waterhouse, N. E.; Rothstein, J. P. Drag Reduction in Turbulent Flows over Superhydrophobic Surfaces. *Phys. Fluids* **2009**, *21*, 085103.

(4) Xue, Y.; Lv, P.; Lin, H.; Duan, H. Underwater Super-hydrophobicity: Stability, Design and Regulation, and Applications. *Appl. Mech. Rev.* **2016**, *68*, 030803.

(5) Marmur, A. Super-Hydrophobicity Fundamentals: Implications to Biofouling Prevention. *Biofouling* **2006**, *22*, 107−115.

(6) Genzer, J.; Efimenko, K. Recent Developments in Super-hydrophobic Surfaces and Their Relevance to Marine Fouling: A Review. *Biofouling* **2006**, *22*, 339−360.

(7) Jeong, C.; Lee, J.; Sheppard, K.; Choi, C.-H. Air-Impregnated Nanoporous Anodic Aluminum Oxide Layers for Enhancing the Corrosion Resistance of Aluminum. *Langmuir* **2015**, *31*, 11040−11050.

(8) Isimjan, T. T.; Wang, T.; Rohani, S. A Novel Method to Prepare Superhydrophobic, UV Resistance and Anti-Corrosion Steel Surface. *Chem. Eng. J.* **2012**, *210*, 182−187.

(9) Barthlott, W.; Neinhuis, C. Purity of the Sacred Lotus, or Escape from Contamination in Biological Surfaces. *Planta* **1997**, *202*, 1−8.

(10) Lv, P.; Xue, Y.; Shi, Y.; Lin, H.; Duan, H. Metastable States and Wetting Transition of Submerged Superhydrophobic Structures. *Phys. Rev. Lett.* **2014**, *112*, 196101.

(11) Forsberg, P.; Nikolajeff, F.; Karlsson, M. Cassie−Wenzel and Wenzel−Cassie Transitions on Immersed Superhydrophobic Surfaces under Hydrostatic Pressure. *Soft Matter* **2011**, *7*, 104−109.

(12) Xiang, Y.; Xue, Y.; Lv, P.; Li, D.; Duan, H. Influence of Fluid Flow on the Stability and Wetting Transition of Submerged Superhydrophobic Surfaces. *Soft Matter* **2016**, *12*, 4241−4246.

(13) Dilip, D.; Bobji, M.; Govardhan, R. N. Effect of Absolute Pressure on Flow through a Textured Hydrophobic Microchannel. *Microfluid. Nanofluid.* **2015**, *19*, 1409−1427.

(14) Poetes, R.; Holtzmann, K.; Franze, K.; Steiner, U. Metastable Underwater Superhydrophobicity. *Phys. Rev. Lett.* **2010**, *105*, 166104.

(15) Bobji, M. S.; Kumar, S. V.; Asthana, A.; Govardhan, R. N. Underwater Sustainability of the "Cassie" State of Wetting. *Langmuir* **2009**, *25*, 12120−12126.

(16) Barthlott, W.; Schimmel, T.; Wiersch, S.; Koch, K.; Brede, M.; Barczewski, M.; Walheim, S.; Weis, A.; Kaltenmaier, A.; Leder, A.; Bohn, H. F. The *Salvinia* Paradox: Superhydrophobic Surfaces with Hydrophilic Pins for Air Retention under Water. *Adv. Mater.* **2010**, *22*, 2325−2328.

(17) Mayser, M. J.; Barthlott, W. Layers of Air in the Water beneath the Floating Fern *Salvinia* are Exposed to Fluctuations in Pressure. *Integr. Comp. Biol.* **2014**, *54*, 1001−1007.

(18) Xiang, Y.; Huang, S.; Huang, T.-Y.; Dong, A.; Cao, D.; Li, H.; Xue, Y.; Lv, P.; Duan, H. Superrepellency of Underwater Hierarchical Structures on *Salvinia* Leaf. *Proc. Natl. Acad. Sci. U.S.A.* **2020**, *117*, 2282−2287.

(19) Gandyra, D.; Walheim, S.; Gorb, S.; Ditsche, P.; Barthlott, W.; Schimmel, T. J. S. Air Retention under Water by the Floating Fern *Salvinia*: The Crucial Role of a Trapped Air Layer as a Pneumatic Spring. *Small* **2020**, *16*, 2003425.

(20) Bing, W.; Wang, H.; Tian, L.; Zhao, J.; Jin, H.; Du, W.; Ren, L. Large Effect: Functional Surfaces Inspired by *Salvinia* Leaves. *Small Struct.* **2021**, *2*, 2100079.

(21) Tricinci, O.; Terencio, T.; Mazzolai, B.; Pugno, N. M.; Greco, F.; Mattoli, V. 3D Micropatterned Surface Inspired by *Salvinia* Molesta *via* Direct Laser Lithography. *ACS Appl. Mater. Interfaces* **2015**, *7*, 25560−25567.

(22) Yang, Y.; Li, X.; Zheng, X.; Chen, Z.; Zhou, Q.; Chen, Y. 3D-Printed Biomimetic Super-Hydrophobic Structure for Microdroplet Manipulation and Oil/Water Separation. *Adv. Mater.* **2018**, *30*, 1704912.

(23) Hunt, J.; Bhushan, B. Nanoscale Biomimetics Studies of *Salvinia* Molestafor Micropattern Fabrication. *J. Colloid Interface Sci.* **2011**, *363*, 187−192.

(24) Zheng, D.; Jiang, Y.; Yu, W.; Jiang, X.; Zhao, X.; Choi, C.-H.; Sun, G. *Salvinia*-Effect-Inspired "Sticky" Superhydrophobic Surfaces by Meniscus-Confined Electrodeposition. *Langmuir* **2017**, *33*, 13640−13648.

(25) Chen, C. S.; Breslauer, D. N.; Luna, J. I.; Grimes, A.; Chin, W. C.; Lee, L. P.; Khine, M. Shrinky-Dink Microfluidics: 3D Polystyrene Chips. *Lab Chip* **2008**, *8*, 622−624.

(26) Zhang, Y.; Li, Y.; Hu, Y.; Zhu, X.; Huang, Y.; Zhang, Z.; Rao, S.; Hu, Z.; Qiu, W.; Wang, Y.; Li, G.; Yang, L.; Li, J.; Wu, D.; Huang, W.; Qiu, C.; Chu, J. Localized Self-Growth of Reconfigurable Architectures Induced by a Femtosecond Laser on a Shape-Memory Polymer. *Adv. Mater.* **2018**, *30*, 1803072.

(27) Yang, Y.; Zhang, Y.; Hu, Y.; Li, G.; Zhang, C.; Song, Y.; Li, L.; Ni, C.; Dai, N.; Cai, Y.; Li, J.; Wu, D.; Chu, J. Femtosecond Laser Regulated Ultrafast Growth of Mushroom-Like Architecture for Oil Repellency and Manipulation. *Nano Lett.* **2021**, *21*, 9301−9309.

(28) Zhao, Y.; Su, Y.; Hou, X.; Hong, M. Directional Sliding of Water: Biomimetic Snake Scale Surfaces. *Opto-Electron. Adv.* **2021**, *4*, 210008.

(29) Zhu, L.; Zhang, Y.-L.; Sun, H.-B. MiniaturisingArtificial Compound Eyes based on Advanced MicronanofabricationTechniques. *Light Adv. Manuf.* **2021**, *2*, 84−100.

(30) Bai, S.; Sugioka, K. Recent Advances in the Fabrication of Highly Sensitive Surface-Enhanced Raman Scattering Substrates: Nanomolar to Attomolar Level Sensing. *Light Adv. Manuf.* **2021**, *2*, 13.

(31) Gandyra, D.; Walheim, S.; Gorb, S.; Barthlott, W.; Schimmel, T. The Capillary Adhesion Technique: A Versatile Method for Determining the Liquid Adhesion Force and Sample Stiffness. *Beilstein J. Nanotechnol.* **2015**, *6*, 11−18.